machines

MDPI

Article

A Novel Measurement-Based Computational Method for Real-Time Distribution of Lateral Wheel–Rail Contact Forces

Nihat Bulduk [1,2] and Muzaffer Metin [2,*]

[1] Vocational School, Istanbul Beykent University, Istanbul 34398, Turkey; nihatbulduk@beykent.edu.tr
[2] Faculty of Mechanical Engineering, Yildiz Technical University, Istanbul 34349, Turkey
* Correspondence: mmetin@yildiz.edu.tr

Abstract

This study has developed a novel measurement-based computational method that accurately determines the vertical and lateral wheel–rail contact forces transmitted from railway vehicles to the rails. A major contribution—and the first in the literature—is the analytical distribution of the total lateral wheelset force into its outer-wheel and inner-wheel components, thereby enabling precise individual evaluation of derailment risk on each wheel in curved tracks. Analytical equations derived from Newton's second law were first formulated to express both vertical forces and total axle lateral force directly from bogie/axle-box accelerations and suspension reactions. To eliminate the deviations caused by conventional simplifying assumptions (neglect of creep effects, wheel diameter variation, and constant contact geometry), surrogate functions and distribution equations sensitive to curve radius, vehicle speed, and cant deficiency were introduced for the first time and seamlessly integrated into the equations. Validation was performed using the Istanbul Tramway multibody model in SIMPACK 2024x.2, with the equations implemented in MATLAB/Simulink R2024b. Excellent agreement with SIMPACK reference results was achieved on straight tracks and curves, after regression-based calibration of the surrogate functions. Although the method requires an initial regression calibration within a simulation environment, it relies exclusively on measurable parameters, ensuring low cost, full compatibility with existing vehicle sensors, and genuine suitability for real-time monitoring. Consequently, it supports predictive maintenance and proactive safety management while overcoming the practical limitations of instrumented wheelsets and offering a robust, fleet-scalable alternative for the railway industry.

Keywords: railway; contact force; wheel–rail contact; safety; dynamic simulation; real-time monitoring; computational method; instrumented wheelset; SIMPACK; surrogate function

check for updates

Academic Editor: Dan Zhang

Received: 7 November 2025
Revised: 23 November 2025
Accepted: 27 November 2025
Published: 28 November 2025

Citation: Bulduk, N.; Metin, M. A Novel Measurement-Based Computational Method for Real-Time Distribution of Lateral Wheel–Rail Contact Forces. *Machines* **2025**, *13*, 1105. https://doi.org/10.3390/machines13121105

Copyright: © 2025 by the authors. Licensee MDPI, Basel, Switzerland. This article is an open access article distributed under the terms and conditions of the Creative Commons Attribution (CC BY) license (https://creativecommons.org/licenses/by/4.0/).

1. Introduction

The vertical and lateral wheel–rail contact forces generated during railway vehicle motion are primary determinants of operational safety. These forces become particularly critical in curved track sections and at high speeds, where they can induce wheel flange climbing and significantly elevate derailment risk. Furthermore, infrastructure- and vehicle-related defects—such as track geometry irregularities, wheel flats, or ballast settlement—frequently cause sudden, high-amplitude spikes in vertical and lateral forces at the contact patch. Such spikes may exceed accepted safety limits and trigger derailment directly. Derailment incidents not only inflict severe damage on vehicles and infrastructure but also lead to catastrophic outcomes, including loss of life and property. International

standards (e.g., EN 14363 [1] and UIC 518 [2]) therefore mandate that the ratio of lateral to vertical wheel–rail forces remains within strictly defined limits. Meanwhile, the ongoing pursuit of higher operating speeds has intensified regulatory requirements concerning noise, vibration, and safety, making accurate real-time determination of wheel–rail contact forces a central focus of contemporary railway research and engineering. This need far exceeds the capabilities of computational analyses and renders precise measurement of dynamic vertical and lateral forces under actual operating conditions indispensable.

The literature on real-time estimation of wheel–rail contact forces from the vehicle side has concentrated around two fundamental methodological groups: (1) direct measurement using strain-gauge-based instrumented wheelsets (IWSs) and (2) indirect or measurement-based computational methods (MBCMs).

Today, the most widely used technique for real-time measurement of vertical and lateral wheel–rail forces is the IWS. Its first series production was initiated in the 1950s by the Swedish company Interfleet [3]. The real breakthrough came in the 2000s. Thanks to advanced signal processing and calibration algorithms applied to strain gauges bonded to the wheel body, high-accuracy real-time data acquisition became possible [4–8].

The core principle of the method is multiple pre-use calibrations of the measuring wheelset to determine the strain-to-load conversion coefficients. However, bonding strain gauges to multiple sections of the wheel is not always feasible due to the structural constraints of the wheel. Therefore, the wheel structure must be subjected to finite element analysis. This analysis identifies the optimum gauge locations that best suit the force calculation methodology [9–13].

Another major source of measurement error is the continuous change in the wheel–rail contact point of contact during vehicle motion. The resulting mass-inertia differences generate errors. Ongoing research aims to minimise these errors (below 10%) through novel approaches such as harmonic cancellation, inverse identification, state-space modelling, and artificial neural networks [8,14–16].

Additionally, rail defects such as corrugation and wheel tread irregularities create high-frequency excitations. These can trigger modal vibrations of the wheelset. Special techniques have been developed to include high-frequency effects in IWS measurements and to minimise related errors [17–20].

In most applications, holes are drilled into the wheel body [21] and strain gauges are installed. The wheelset must be calibrated before commissioning. Static loading is insufficient for calibration. Instead, expensive dynamic roller rigs are typically employed [22].

Although the IWS method has gained widespread acceptance, particularly in vehicle/track type approval testing, due to its high accuracy achieved through historical development, it is not considered suitable for continuous use in predictive maintenance and performance monitoring on a single vehicle set. The strain gauges on the IWS rotate at high speed together with the wheels. Real-time data acquisition from a high-speed rotating wheel requires a telemetry system. Some components of this system, mounted on the axle, rotate with the wheel. Providing long-term stability of these rotating components is extremely challenging.

The practical limitations of instrumented wheelsets (IWSs) have brought indirect measurement-based computational methods (MBCMs) to the forefront since 2007. These methods estimate contact forces without any intervention in the wheelset. They use data from accelerometers, gyroscopes, and displacement sensors mounted on the axle box, bogie frame, or car body, processed through mathematical models.

The first operational milestone belongs to Matsumoto et al. [23–25]. Their gap-sensor and suspension deflection-based system was pioneering. It evaluated the Nadal criterion dynamically in the time domain, calculated the real-time Y/Q ratio, and transferred de-

railment monitoring to actual revenue-service trains. The method requires neither special wheelsets nor rotating telemetry. It directly measures wheel lateral distortion with non-contact gap sensors while estimating vertical and longitudinal forces from primary suspension deflections. Verified on Tokyo Metro commercial lines and a full-scale bogie test stand, it is recognized as the first practical MBCM system suitable for continuous monitoring.

This pioneering approach laid the foundation for subsequent inverse dynamic model-based methods. Wei et al. [26] proposed a more advanced inverse model. Using axle-box strains, accelerometers, and primary suspension displacement sensors, they estimated the total axle lateral force (H) and individual wheel vertical forces (Qi) separately. Treating the wheelset as rigid, they solved the force and moment equilibrium equations. Field tests on the Beijing Loop (1300 m radius curve) achieved lateral force estimation errors below 10% when compared to IWS measurements.

After 2015, Kalman filter-based observers [27–29] and frequency-domain deconvolution of axle-box accelerations [30,31] provided significant improvements in real-time noise suppression and high-frequency event detection. However, they remained insufficient for quasi-static curving forces and parameter variations.

More recently, hybrid and data-driven approaches have become dominant. Bosso and Zampieri [32] substantially reduced computation time with fast tangential force algorithms alternative to FASTSIM/Polach. Pires et al. [33], Gadhave and Vyas [34], Majumder et al. [35], Zhu et al. [36], and Liu et al. [37] achieved high accuracy using artificial neural networks and automated machine learning, largely solving generalization issues across speed, curve radius, and cant deficiency. Nevertheless, these methods still require lengthy testing or simulation-based algorithm training.

Despite these advances, most existing MBCMs share common weaknesses: neglect of creep effects and excessive linearization, estimation of only total axle lateral force in curves (no distribution of outer/inner wheel lateral forces), insufficient generalization across parameters, dependency on track irregularity inputs or extensive training datasets, and high online computational burden.

On the other hand, wayside methods, which involve placing strain gauges on the rails for point-based load measurement, are not suitable for online monitoring and therefore remain outside the scope of this study. However, when properly applied, they can yield highly realistic results. In this context, Cortis et al. [38] compared indirect and wayside methods at a single point and reported that the indirect method operated with approximately 10% error. This finding is valuable as it reflects the shortcomings of the indirect method used in that study.

This study proposes a new low-cost, online-monitoring-compatible MBCM that addresses these chronic gaps in the literature while requiring only simple acceleration and displacement sensors. Unlike most similar methods in the literature, which rely on simple mathematical equations transferring measurable loads from acceleration and suspension sources to the rail, the proposed approach avoids approximations such as neglecting creep effects, excessive linearizations, and assuming constant contact geometry—approximations that limit physical fidelity and cause deviations from real data.

Building on Wei et al. [26], analytical force equations derived from Newton's second law are used to express vertical forces and total axle lateral force (H) directly in terms of bogie/axle-box accelerations and suspension forces. Using data from the local Istanbul Tramway (ITA) model in SIMPACK (the vehicle developed by Metro Istanbul A.Ş. and commissioned in 2014), the equations implemented in MATLAB/Simulink are enriched with surrogate functions (SFs) capable of operating under varying curve radii, vehicle speeds, and cant deficiencies, thereby minimizing the drawbacks of existing approaches.

The most important novelty of the study is the analytical distribution of outer- and inner-wheel lateral forces, which is generally neglected in the literature. New equations based on curve radius, cant deficiency, and vehicle speed enable high-accuracy evaluation of flange climb risk at each contact point separately. Both the surrogate-enhanced force equations and the lateral force distribution approach have been comprehensively validated against outputs from SIMPACK, today's most widely used multibody dynamics software in railway simulations. Nearly identical results were obtained from straight tracks to sharp curves, raising initial deviations to a high level of consistency. These aspects also highlight the distinctions from the authors' previous work [39].

In conclusion, the proposed method offers a low-cost, highly generalizable, and sustainable alternative by effectively utilizing existing sensor infrastructure. It provides tangible contributions to fleet-scale continuous derailment risk monitoring, predictive maintenance, and performance optimization while overcoming the practical limitations of instrumented wheelsets and elevating railway operational safety to a new level.

2. Methods

In this section, to validate the reliability of the developed analytical methods, the reference vehicle—ITA—was modeled in SIMPACK, a widely used multibody dynamics simulation software. Subsequently, equations for vertical and lateral forces transmitted from the railway vehicle to the rails, as reported in the literature [26], were re-derived considering the kinematics of ITA. SFs capable of producing more accurate results across varying curve radii, vehicle speeds, and cant deficiencies were developed and integrated into the force transmission equations. Finally, the total lateral forces transmitted from the wheels to the rail in curves were distributed into right and left contact points using equations proposed for the first time in this study.

2.1. Multibody Dynamics Simulation Environment: SIMPACK

To evaluate the accuracy of the developed mathematical model, SIMPACK—a widely used multibody dynamics simulation software capable of realistically modeling all railway vehicle components and environmental factors—was selected. This software enables detailed dynamic analyses under varying vehicle speeds and track conditions, accurately simulating wheel–rail contact using advanced physical algorithms (e.g., Hertz contact, Kalker theory), thereby producing reliable results with low error margins for contact forces, vibration, and safety parameters. SIMPACK's ability to model not only rail systems but also other dynamic systems realistically has established it as a standard tool in numerous industrial projects and academic studies. Accordingly, consistent with the works cited in the introduction [26,27,34,36], the consistency of the analytical model in this research is validated using SIMPACK.

The reference vehicle modeled in this study is an ITA articulated tram, consisting of a total of six wheelsets, three bogies and two car bodies connected by articulation joints. The detailed multibody model, implemented in SIMPACK, comprises 734 degrees of freedom and accurately represents the real vehicle. The central bogie serves as a non-powered carrying (trailer) bogie, whereas the two end bogies are powered (motorized) traction bogies. The vehicle is equipped with a two-stage suspension system (primary and secondary) and operates as an urban light-rail tram (Figure 1). Key defining parameters of the vehicle are presented in Table 1.

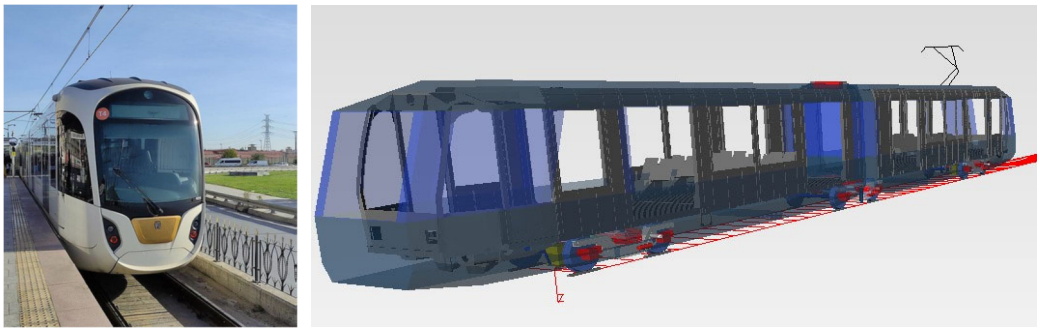


Figure 1. ITA tram vehicle and its SIMPACK model.

Table 1. Railway vehicle system parameters [39].

Parameter	Description	Unit
Nominal wheel radius	0.35	[m]
Lateral wheel spacing	0.75	[m]
Track gauge	1435	[mm]
Dynamic friction coefficient	0.32	-
Static friction coefficient	0.4	-
Distance between bogies	8.6	[m]
Vehicle height	3.5	[m]
Vehicle width	2.65	[m]
Vehicle length	19.45	[m]
Total vehicle mass	35,000	[kg]

Examination of the SIMPACK algorithm reveals that numerous parameters (contact angle, conicity, friction, elasticity, etc.) are interdependent, and incorporating creep effects into the equations is essential for determining instantaneous loads. However, the measurement difficulties and computational complexity of these parameters impose significant limitations on practical applications.

2.2. Theoretical Framework of Contact Force Equations for MBCM

In this section, the equations for vertical and lateral forces transmitted from the railway vehicle to the rails on straight tracks and curves are re-derived, taking into account the kinematics of ITA.

2.2.1. Wheel–Rail Vertical and Lateral Contact Forces on Straight Tracks

In this study, since the objective is to derive dynamic force equations based solely on parameters obtainable through indirect measurement methods, the vertical contact forces acting on the wheelset under straight-track conditions were determined using Newton's second law. Moment equilibrium equations were established on the wheelset free-body diagram presented in Figure 2, incorporating suspension forces and inertial forces. Subsequent algebraic manipulations yielded the final expressions for the outer and inner wheel vertical contact forces, given in Equations (1) and (2), respectively.

$$F_{z_{out}} = \left(\left(m_w \ddot{z}_{wi} + m_w g \right) \frac{1}{2} - \left(m_w \ddot{y}_{wi} + F_{sy_{in}} + F_{sy_{out}} \right) \frac{r_0}{L_c} + F_{sz_{out}} \frac{(L_s + L_c)}{2L_c} - F_{sz_{in}} \frac{(L_s - L_c)}{2L_c} \right) \tag{1}$$

$$F_{z_{in}} = \left(\left(m_w \ddot{z}_{wi} + m_w g \right) \frac{1}{2} + \left(m_w \ddot{y}_{wi} + F_{sy_{in}} + F_{sy_{out}} \right) \frac{r_0}{L_c} - F_{sz_{out}} \frac{(L_s - L_c)}{2L_c} + F_{sz_{in}} \frac{(L_s + L_c)}{2L_c} \right) \tag{2}$$

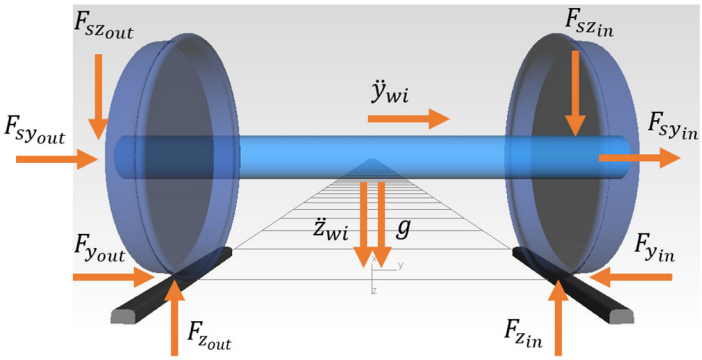


Figure 2. Free-body diagram of wheelset on straight track.

The primary vertical and lateral suspension force equations acting on the outer and inner wheels of the wheelset are derived as presented in Equations (3) and (4), respectively.

$$\begin{aligned} F_{sz_{out}} = F_{szin} = K_{pz}(z_{wi} - z_{ti}) + K_{pz}\tfrac{L_s}{2}(\varnothing_{wi} - \varnothing_{ti}) + K_{pz}L_1\beta_{ti} \\ +C_{pz}(\dot{z}_{wi} - \dot{z}_{ti}) + C_{pz}\tfrac{L_s}{2}\left(\dot{\varnothing}_{wi} - \dot{\varnothing}_{ti}\right) + C_{pz}L_1\dot{\beta}_{ti} + F_{sz_{static}} \end{aligned} \tag{3}$$

$$\begin{aligned} F_{sy_{out}} = F_{sy_{in}} = K_{py}(y_{wi} - y_{ti}) + K_{py}L_1\psi_{ti} - K_{py}h_t\phi_{ti} \\ +C_{py}(\dot{y}_{wi} - \dot{y}_{ti}) + C_{py}L_1\dot{\psi}_{ti} - C_{py}h_t\dot{\phi}_{ti} \end{aligned} \tag{4}$$

In railway vehicles traveling on straight tracks, lateral contact forces arise due to primary lateral suspension forces and wheelset lateral inertial forces. In this study, a force equilibrium equation was established on the free-body diagram in Figure 2 in accordance with Newton's second law, yielding the preliminary expression in Equation (5). Following the necessary algebraic manipulations, the final form of the total lateral contact force is presented in Equation (8).

$$m_w\ddot{y}_{wi} + F_{sy_{in}} + F_{sy_{out}} - F_{y_{in}} + F_{y_{out}} = 0 \tag{5}$$

Here, F_{syi} represents the total primary lateral suspension force, and (H) denotes the total lateral wheel–rail contact force, expressed as in Equations (6) and (7).

$$F_{syi} = F_{sy_{in}} + F_{sy_{out}} \tag{6}$$

$$H = F_{y_{in}} - F_{y_{out}} \tag{7}$$

By rearranging the force equation given in Equation (5) according to the parameters in Equations (6) and (7), the final form of the total lateral wheel–rail contact force equation is obtained as presented in Equation (8).

$$H = m_w\ddot{y}_{wi} + F_{syi} \tag{8}$$

The descriptions of the notations used in the presented equations are given in Appendix A Table A1 under the nomenclature section.

2.2.2. Wheel–Rail Vertical and Lateral Contact Forces in Curves

When a railway vehicle travels in a curve, the vertical forces transmitted from the wheels to the rails differ from those on straight tracks due to the influence of centrifugal force. This force causes the vehicle to tend to shift outward along the curve, resulting in an increase in vertical contact force at the outer wheel and a decrease at the inner wheel. In this study, vertical contact forces were determined using Newton's second law, accounting for centrifugal effects. Moment equilibrium equations were established on the wheelset

free-body diagram shown in Figure 3, yielding the final expressions for the outer and inner wheel vertical contact forces in Equations (9) and (10), respectively.

$$F_{z_{out}} = \left(m_w\left(\ddot{z}_{wi} + \frac{V^2 sin\ \varnothing_{se}}{R} + gcos\ \varnothing_{se}\right)\frac{1}{2} - \left(m_w\ddot{y}_{wi} + F_{sy_{in}} + F_{sy_{out}}\right)\frac{r_0}{L_c}\right.$$
$$\left. + m_w\left(\frac{V^2 cos\ \varnothing_{se}}{R} - gsin\ \varnothing_{se}\right)\frac{r_0}{L_c} + F_{sz_{out}}\frac{(L_s+L_c)}{2L_c} - F_{sz_{in}}\frac{(L_s-L_c)}{2L_c}\right) \quad (9)$$

$$F_{z_{in}} = \left(m_w\left(\ddot{z}_{wi} + \frac{V^2 sin\ \varnothing_{se}}{R} + gcos\ \varnothing_{se}\right)\frac{1}{2} + \left(m_w\ddot{y}_{wi} + F_{sy_{in}} + F_{sy_{out}}\right)\frac{r_0}{L_c}\right.$$
$$\left. - m_w\left(\frac{V^2 cos\ \varnothing_{se}}{R} - gsin\ \varnothing_{se}\right)\frac{r_0}{L_c} - F_{sz_{out}}\frac{(L_s-L_c)}{2L_c} + F_{sz_{in}}\frac{(L_s+L_c)}{2L_c}\right) \quad (10)$$

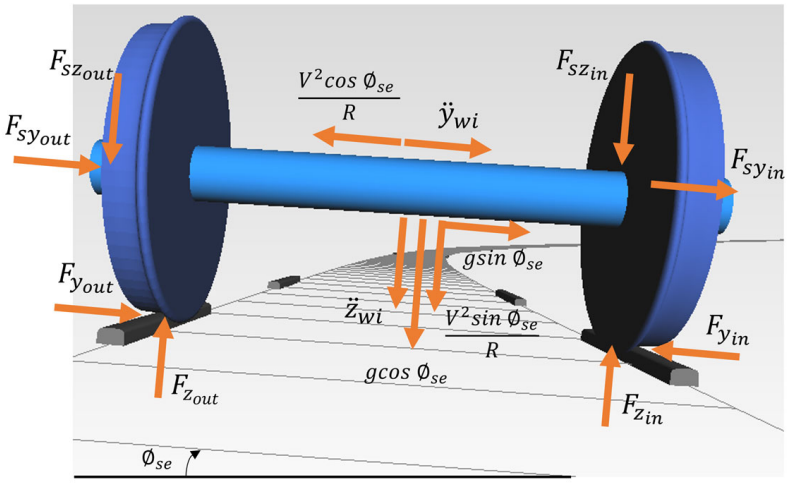


Figure 3. Free-body diagram of a wheel set on a curve.

In a railway vehicle traveling in a curve, centrifugal force arises due to the turn at a specific radius, altering the lateral contact forces on the wheelset. In this study, accounting for the centrifugal effect, a force equilibrium equation was established on the free-body diagram in Figure 3, yielding the preliminary expression in Equation (11). Following the necessary manipulations, the final form of the total lateral contact force is presented in Equation (14).

$$m_w\left(\ddot{y}_{wi} - \frac{V^2}{R}cos\ \phi_{se} + gsin\ \phi_{se}\right) + F_{sy_{in}} + F_{sy_{out}} - F_{y_{in}} + F_{y_{out}} = 0 \quad (11)$$

Here, F_{syi}, represents the total primary lateral suspension force, and H denotes the total lateral wheel–rail contact force, expressed as in Equations (12) and (13).

$$F_{syi} = F_{sy_{in}} + F_{sy_{out}} \quad (12)$$

$$H = F_{y_{in}} - F_{y_{out}} \quad (13)$$

By rearranging the force equation given in Equation (11) according to the parameters in Equations (12) and (13), the final form of the total lateral wheel–rail contact force equation is obtained as presented in Equation (14).

$$H = m_w\left(\ddot{y}_{wi} - \frac{V^2}{R}cos\ \phi_{se} + gsin\ \phi_{se}\right) + F_{syi} \quad (14)$$

2.3. Development of Surrogate Functions (SFs) for Vertical and Lateral Wheel–Rail Contact Forces

To mitigate dynamic limitations in the real-time MBCM—such as neglected creep effects in the contact patch and variable wheel diameter—lateral and vertical SFs have been integrated into the total lateral and vertical contact force equations. These functions were developed using the least-squares method to achieve higher agreement with SIMPACK simulation results.

The primary reason for selecting the least-squares method is its effectiveness as a regression technique that minimizes the sum of squared errors between SIMPACK outputs and analytical model predictions to determine the coefficients.

In this context, discrepancies between the total lateral and vertical contact force data from SIMPACK simulations and the analytical model outputs were analyzed. The coefficients k_t, g_t, z_t and k_{td}, g_{td}, z_{td} in the SF equations incorporating vehicle speed, curve radius, and cant deficiency (Equations (15) and (16)) were determined through error minimization.

$$F_{y_v} = k_t V^2 + g_t V^2 R + z_t d \tag{15}$$

$$F_{z_{v(out,in)}} = k_{td(out,in)} V + g_{td(out,in)} VR + z_{td(out,in)} d \tag{16}$$

Here, F_{y_v} represents the lateral SF, $F_{z_{v(out,in)}}$ the outer and inner vertical SFs, V the vehicle speed (km/h), R the curve radius in meters, and d the cant deficiency in mm. The objective of the regression analysis is to make the values of F_{y_v} and F_{z_v} as close as possible to the corresponding F_{y_r} and F_{z_r} values obtained from SIMPACK simulations. Within this framework, the solution steps of the least-squares method used to determine the coefficients in the lateral SF are provided in Equations (17)–(24).

Independent variables:

$$x_1 = V^2 \tag{17}$$

$$x_2 = V^2 R \tag{18}$$

$$x_3 = d \tag{19}$$

Dependent variables:

$$y_t = k_t x_1 + g_t x_2 + z_t x_3 \tag{20}$$

Error function:

$$S = \sum (y_{ri} - (k_t x_{1i} + g_t x_{2i} + z_t x_{3i}))^2 \tag{21}$$

Minimization:

$$\frac{\partial S}{\partial k_t} = 0, \ \frac{\partial S}{\partial g_t} = 0, \ \frac{\partial S}{\partial z_t} = 0 \tag{22}$$

As can be seen above, the coefficients are obtained for values that reduce the errors to zero. In Equations (23) and (24), the normal equations are formulated for the lateral SF based on the dependent and independent variables:

$$A^T A \cdot [k_t \ g_t \ \ z_t \ ] = A^T b$$
$$A = \begin{bmatrix} x_{11} \ x_{21} \ x_{31} & x_{12} \ x_{22} \ x_{32} & \vdots \ x_{1n} \ \vdots \ x_{2n} & \vdots \ x_{3n} \end{bmatrix}, \ b = \begin{bmatrix} y_{r1} \ y_{r2} \vdots \ y_{rn} \end{bmatrix} \tag{23}$$

Calculation of coefficients:

$$[k_t \ g_t \ z_t \ ] = \left(A^T A\right)^{-1} \cdot A^T b \tag{24}$$

The solution matrix for calculating the coefficients in the lateral SF is provided in Equation (24), and the coefficients have been computed accordingly. The same procedure was applied to the vertical SF, determining its coefficients. Once the coefficients

for both lateral and vertical SFs were established, they were substituted into the respective SF equations, yielding the final forms of the lateral and vertical SFs as presented in Equations (25) and (26).

Lateral SF:

$$F_{y_v} = -0.1525V^2 + 3.4749 * 10^{-4}V^2R - 5.7190d \quad (25)$$

Vertical SF:

$$\begin{aligned} F_{z_{v,out}} &= -64.5715V + 0.1062VR - 6.533d \\ F_{z_{v,in}} &= 64.5715V - 0.1062VR + 6.533d \end{aligned} \quad (26)$$

The developed lateral and vertical SFs were integrated into the established force equations (Equations (9), (10) and (14)), resulting in the final forms of the total lateral contact force (H_f) and vertical wheel contact force equations ($F_{z_{out,f}}$, $F_{z_{in,f}}$) as presented in Equations (27) and (28). The refined equations were implemented in MATLAB/Simulink and simulated for the test scenarios defined in Table 2. The total lateral and vertical wheel–rail contact forces estimated using the surrogate functions (SFs) were compared with the SIMPACK reference results, following the block diagram presented in Figure 4, to assess the performance of the proposed approach.

$$H_f = H + F_{y_v} \quad (27)$$

$$\begin{aligned} F_{z_{out,f}} &= F_{z_{out}} + F_{z_{v,out}} \\ F_{z_{in,f}} &= F_{z_{in}} + F_{z_{v,in}} \end{aligned} \quad (28)$$

Table 2. Simulation scenarios.

Scenarios	Vehicle Speed (km/h)	Curve Radius (m)	Superelevation (m)
1	15	300	0.052
2	15	89	0
3	25	300	0.052
4	25	89	0

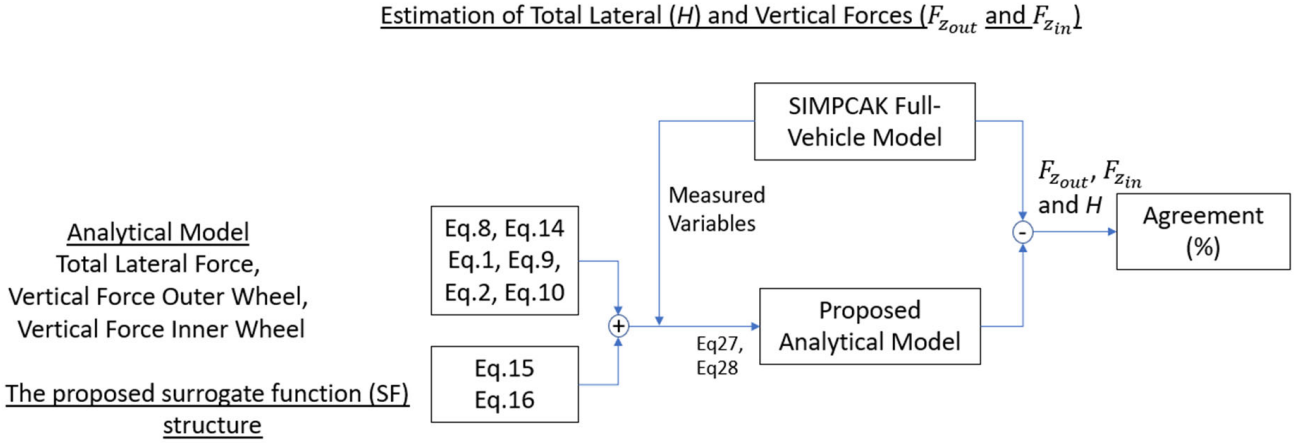


Figure 4. Block diagram for estimating total lateral and vertical forces.

2.4. Distribution of Lateral Wheel–Rail Contact Forces into Inner and Outer Wheel Contact Regions

The force equations developed in the previous section yield only the total lateral contact force acting on the wheelset. This limitation restricts the evaluation of vehicle and track safety criteria defined in EN 14363 and UIC 518 standards (e.g., derailment coefficient and wheel unloading ratio). To overcome this constraint, an analytical approach

is proposed for the first time in this study to distribute lateral contact forces into outer and inner wheel components using MBCMs.

Within this framework, a set of equations defining the relationship between the total lateral force H and its separated components was established. For non-canted and canted curved tracks, outer and inner wheel lateral contact forces were derived using least-squares regression. In the non-canted case, the outer and inner wheel forces are formulated in Equations (29) and (30) as functions of total lateral force, vertical forces, curve radius, and vehicle speed; the coefficients k_{1d}, k_{2d}, k_{1i}, k_{2i} were determined through regression.

$$F_{y_{out}} = H_f + (k_{1d}V + k_{2d}R)\frac{F_{z_{out,f}}}{F_{z_{out,f}} + F_{z_{in,f}}} \tag{29}$$

$$F_{y_{in}} = H_f + (k_{1i}V + k_{2i}R)\frac{F_{z_{in,f}}}{F_{z_{out,f}} + F_{z_{in,f}}} \tag{30}$$

Here, $F_{y_{out}}$ represents the outer wheel lateral contact force on a non-canted track, and $F_{y_{in}}$ denotes the inner wheel lateral contact force. In the canted track case, the outer and inner wheel lateral contact forces are formulated in Equations (31) and (32) as functions of total lateral force, vertical forces, curve radius, vehicle speed, and cant deficiency; the coefficients k_{1dd}, k_{2dd}, k_{1id}, k_{2id}, k_{3d}, k_{3i} were determined using the least-squares method.

$$F_{y_{outd}} = H_f + (k_{1dd}V + k_{2dd}R + k_{3d}d)\frac{F_{z_{out,f}}}{F_{z_{out,f}} + F_{z_{in,f}}} \tag{31}$$

$$F_{y_{ind}} = H_f + (k_{1id}V + k_{2id}R + k_{3i}d)\frac{F_{z_{in,f}}}{F_{z_{out,f}} + F_{z_{in,f}}} \tag{32}$$

Here, $F_{y_{outd}}$ represents the outer wheel lateral contact force on a canted track, and $F_{y_{ind}}$ denotes the inner wheel lateral contact force. The obtained coefficients were substituted into the respective lateral contact force equations, yielding the final expressions for the outer and inner wheel lateral contact forces on non-canted and canted curved tracks as presented in Equations (33)–(36).

$$F_{y_{out}} = H_f + (-1.015V + 0.2425R)\frac{F_{z_{out,f}}}{F_{z_{out,f}} + F_{z_{in,f}}} \tag{33}$$

$$F_{y_{in}} = H_f + (3.8444V - 0.2207R)\frac{F_{z_{in,f}}}{F_{z_{out,f}} + F_{z_{in,f}}} \tag{34}$$

$$F_{y_{outd}} = H_f + (-0.5138V + 0.0339R + 0.23057d)\frac{F_{z_{out,f}}}{F_{z_{out,f}} + F_{z_{in,f}}} \tag{35}$$

$$F_{y_{ind}} = H_f + (0.8099V - 0.0556R - 0.15402d)\frac{F_{z_{in,f}}}{F_{z_{out,f}} + F_{z_{in,f}}} \tag{36}$$

The outputs generated by these equations provide the lateral forces transmitted to the rails from the inner and outer wheel contact points in curved sections. Figure 5 presents the block diagram illustrating how the derived equations are implemented and executed in the MATLAB/Simulink environment.

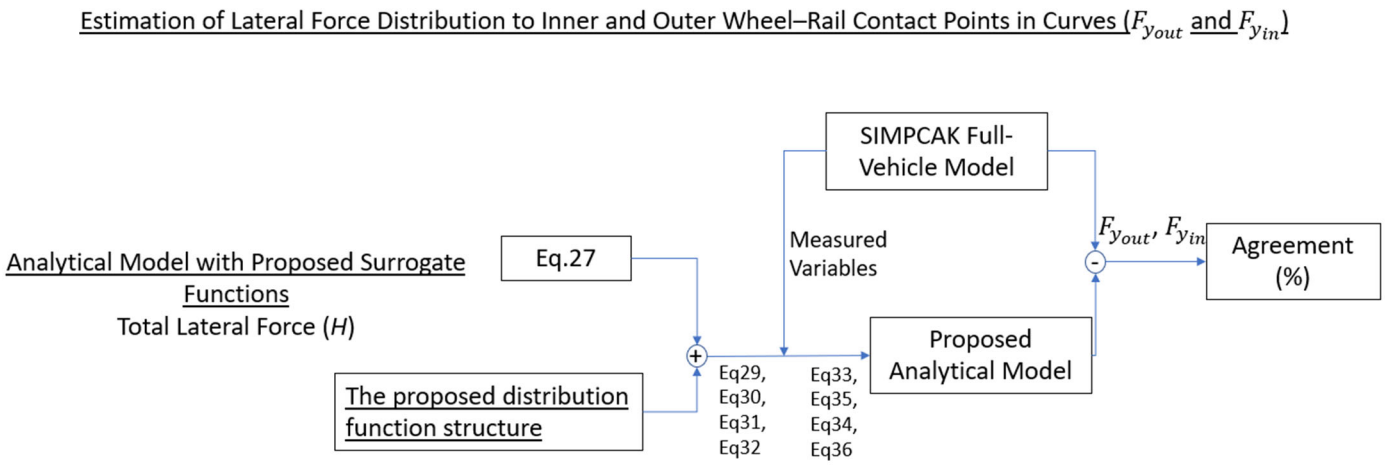


Figure 5. Block diagram for estimating lateral force distribution to inner and outer wheel–rail contacts.

3. Simulation Results

In this section, the performance of the proposed analytical models is evaluated by comparing their outputs with the detailed multibody simulations performed in SIMPACK using the İTA tram as the reference vehicle. To drive the analytical models, inertial accelerations together with suspension displacements and velocities were extracted from the SIMPACK simulations for the scenarios defined in Table 2. These data were then fed into the MATLAB/Simulink implementation of the developed equations, which estimate the real-time lateral and vertical wheel–rail contact forces. The resulting contact force-time outputs and the corresponding agreement metrics are presented and discussed below, with quantitative comparisons summarized in Table 3.

Table 3. Compared models and outputs.

Examined Outputs	Compared Models			Figure Numbers
Total Lateral Force (*H*)	SIMPACK	Analytical Model (Equations (8) and (14))	Analytical Model with SF (Equation (27))	Figures 6–9
Vertical Force Acting on the Inner Wheel	SIMPACK	Analytical Model (Equations (3) and (10))	Analytical Model with SF (Equation (28))	Figures 10–13
Vertical Force Acting on the Outer Wheel	SIMPACK	Analytical Model (Equations (2) and (9))	Analytical Model with SF (Equation (28))	Figures 10–13
Lateral Force Acting on the Inner Wheel	SIMPACK	Distributed Analytical Model (Equations (34) and (36))		Figures 14–17
Lateral Force Acting on the Outer Wheel	SIMPACK	Distributed Analytical Model (Equations (33) and (35))		Figures 14–17

Comparative simulation outcomes reveal that the proposed method operates comprehensively and yields verifiable results on both straight tracks and curves, across different speeds, curve radii, and cant deficiency values.

Upon examination of the graphs in Figures 6–9, the force outputs obtained from SIMPACK are compared with those from the developed analytical method for vehicle speeds of 15 km/h and 25 km/h on curved tracks with radii of 89 m and 300 m.

The results of the study, including the total lateral wheel–rail contact force values and agreement ratios, are presented in Table 4. The agreement ratios presented in all tables were

calculated using the expression given in Equation (37), which is based on the normalized absolute error. Here, n denotes the number of data points utilized.

$$Agreement\ (\%) = \left(1 - \frac{\frac{1}{n}\sum_{i=1}^{n}|SIMPACK\ Data - Proposed\ Model\ Data|}{max(SIMPACK\ Data) - \min(SIMPACK\ Data)}\right) \times 100 \quad (37)$$

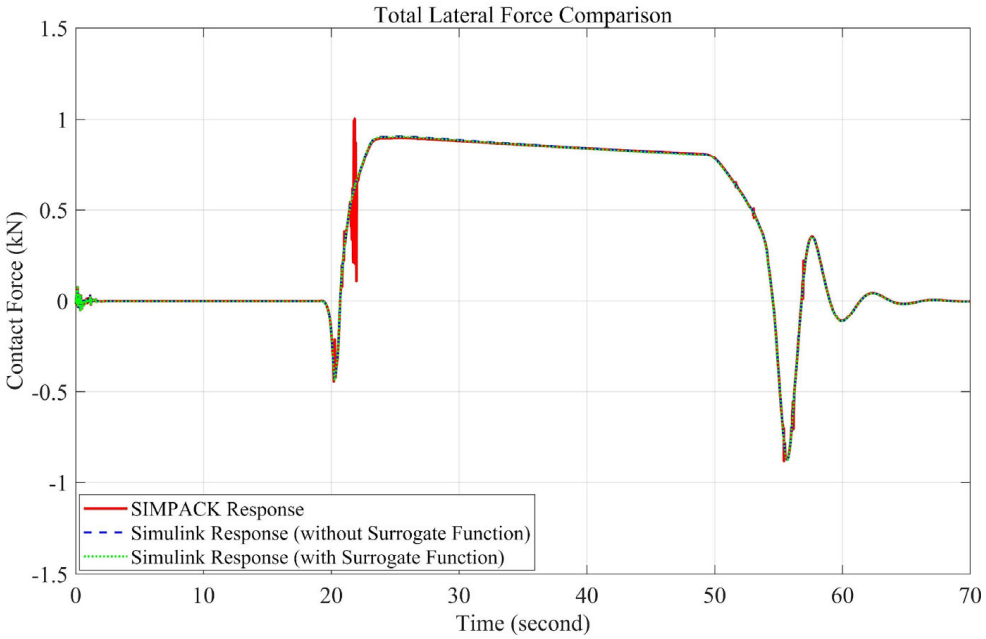


Figure 6. Comparison of total lateral forces for 15 km/h and 89 m curve radius.

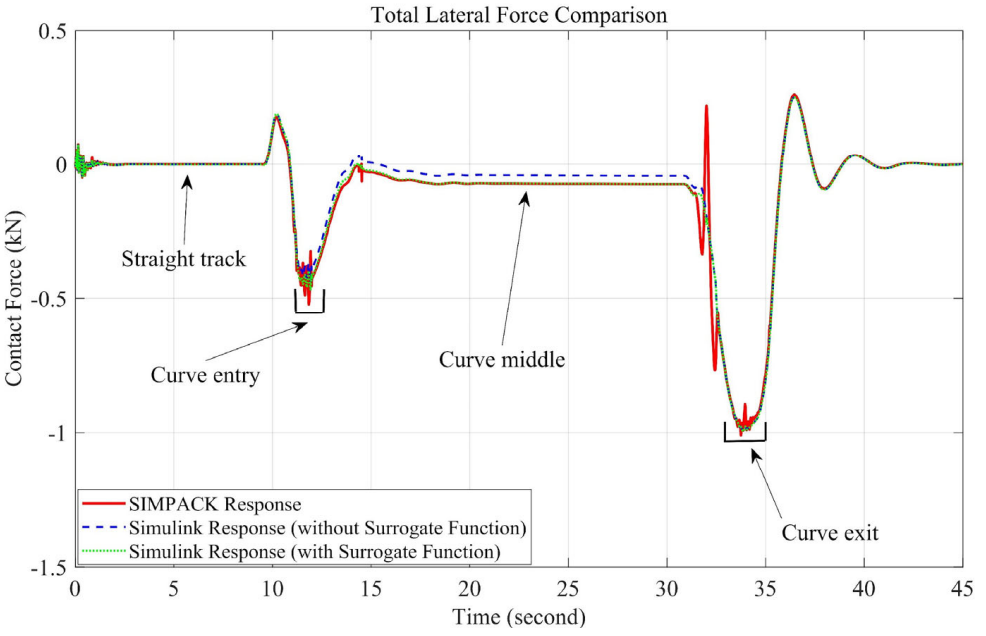


Figure 7. Comparison of total lateral forces for 15 km/h and 300 m curve radius.

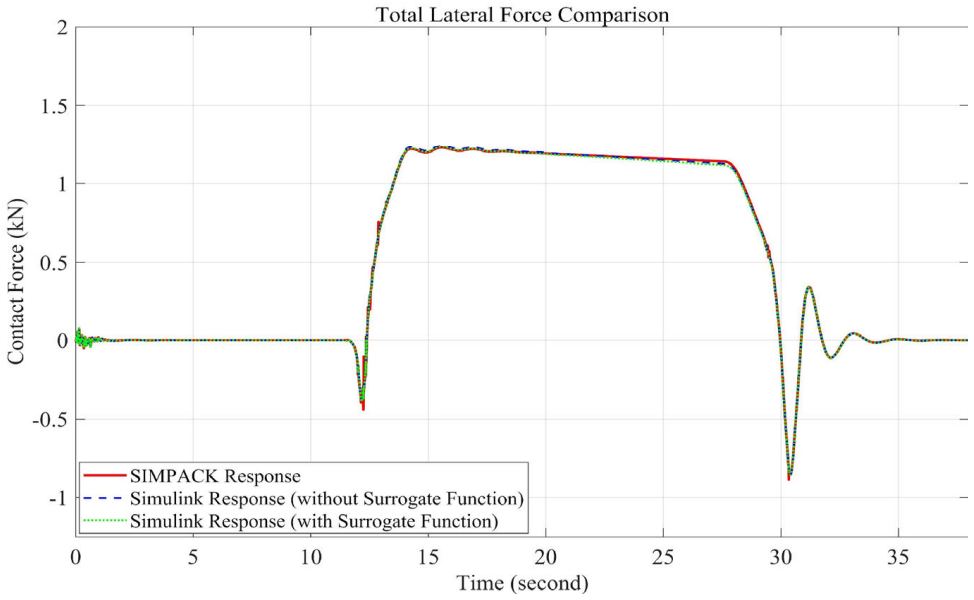


Figure 8. Comparison of total lateral forces for 25 km/h and 89 m curve radius.

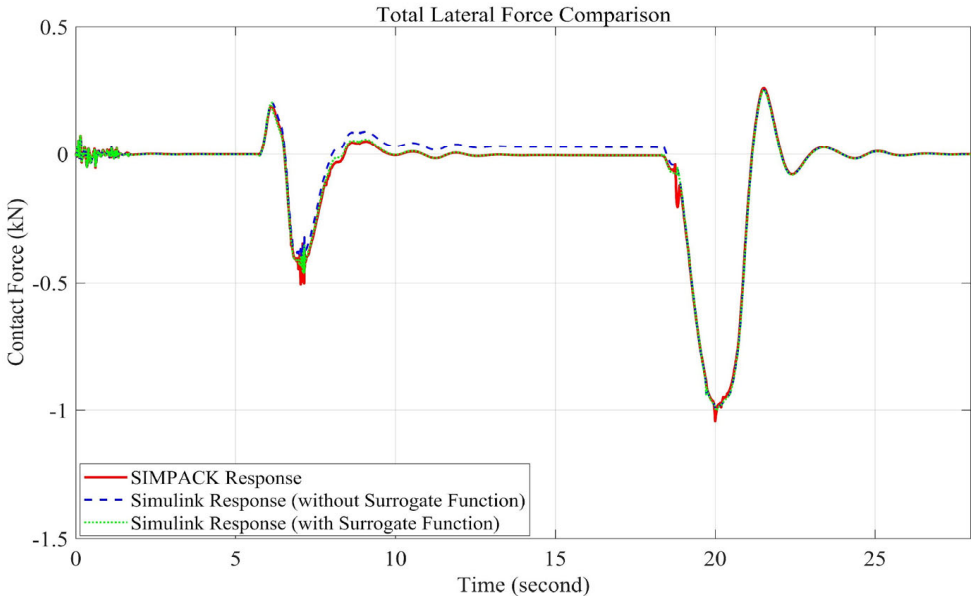


Figure 9. Comparison of total lateral forces for 25 km/h and 300 m curve radius.

Table 4. Comparison of total lateral force (*H*) simulation results.

Simulation Scenarios		Total Lateral Force (*H*) Agreement with SIMPACK Data (%)					
		Tangent Track		Curve		Total Track	
		Without SF	With SF	Without SF	With SF	Without SF	With SF
15 km/h	R = 89 m	99.9	99.9	99.7	99.7	99.8	99.8
	R = 300 m	99.9	99.9	97.4	99.0	99.9	99.9
25 km/h	R = 89 m	99.9	99.9	99.7	99.7	99.8	99.8
	R = 300 m	99.9	99.9	98.1	99.6	98.7	99.7

The proposed SF-based method achieves agreement exceeding 99.7% with the SIMPACK reference in all simulated scenarios. The incorporation of SFs substantially improves accuracy in curved sections, increasing agreement from as low as 97.4% (without SFs) to 99% and above.

Figures 10–13 compare the outer wheel, inner wheel, and total vertical contact force values obtained from SIMPACK with those calculated using the developed vertical contact force equations. The consistency ratios for the outer and inner wheel vertical contact forces are presented in Table 5.

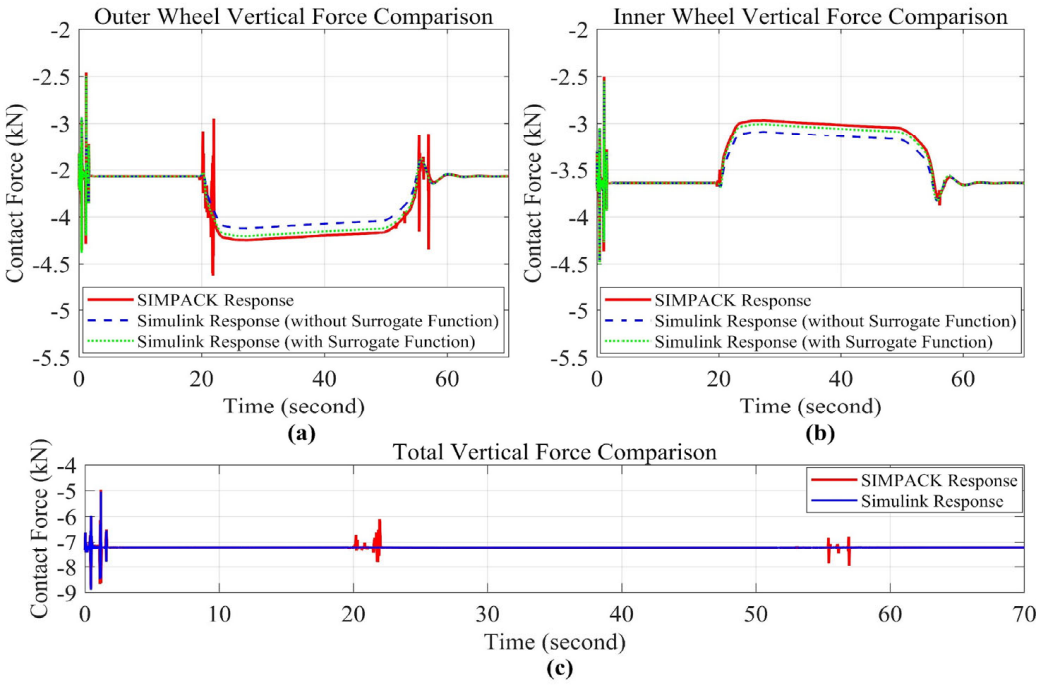


Figure 10. Comparison of vertical wheel forces for 15 km/h and 89 m curve radius: (**a**) outer wheel vertical force comparison; (**b**) inner wheel vertical force comparison; (**c**) total vertical force comparison.

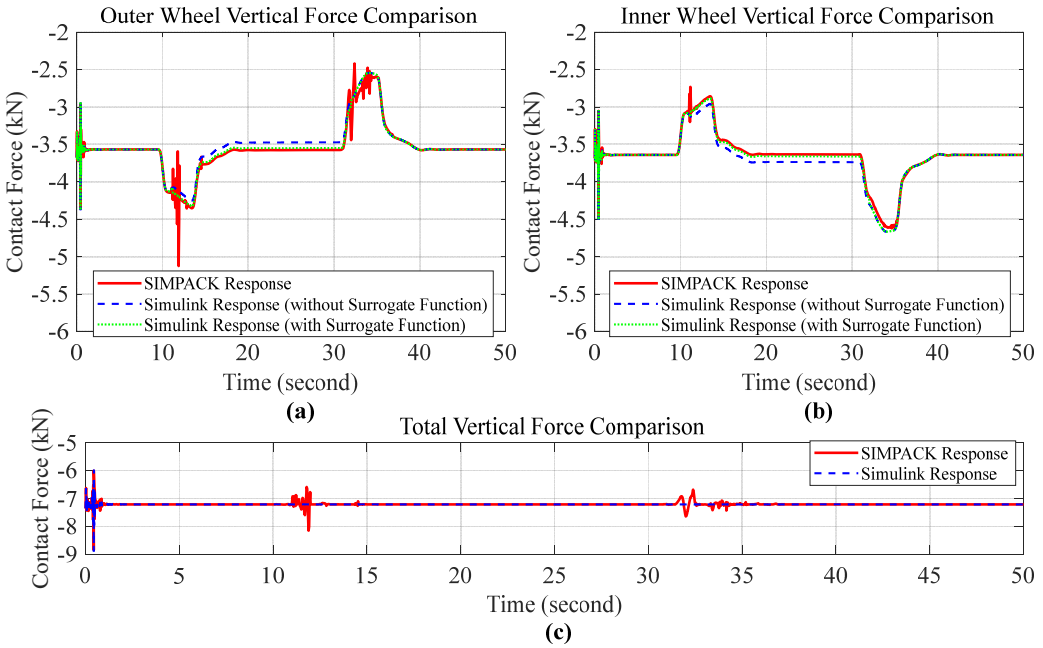


Figure 11. Comparison of vertical wheel forces for 15 km/h and 300 m curve radius: (**a**) outer wheel vertical force comparison; (**b**) inner wheel vertical force comparison; (**c**) total vertical force comparison.

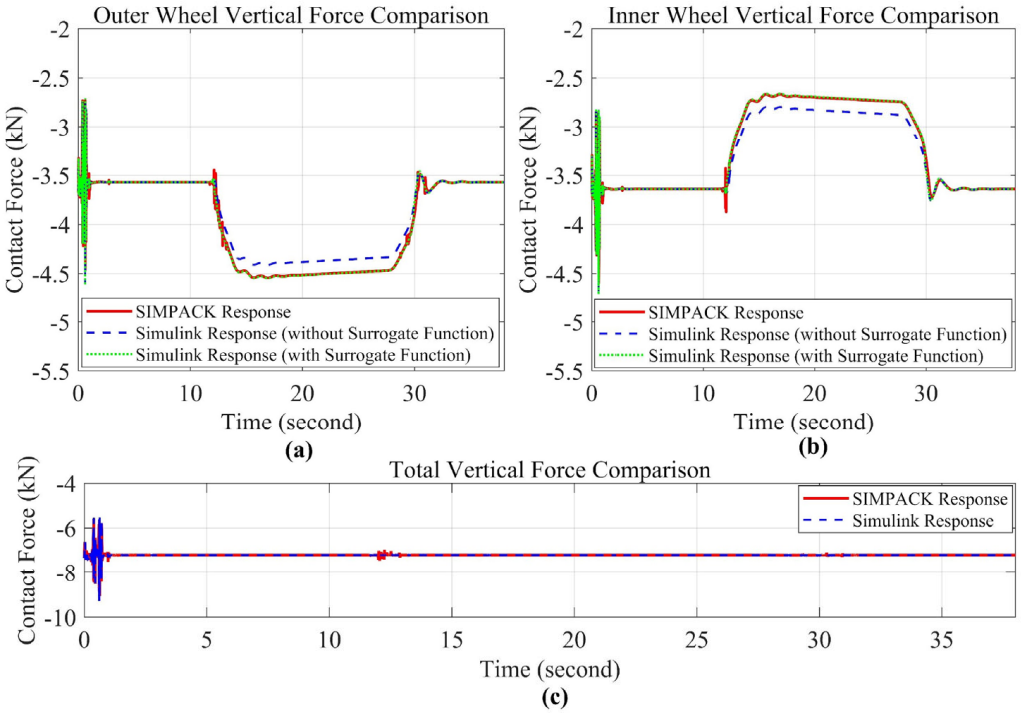


Figure 12. Comparison of vertical wheel forces for 25 km/h and 89 m curve radius: (**a**) outer wheel vertical force comparison; (**b**) inner wheel vertical force comparison; (**c**) total vertical force comparison.

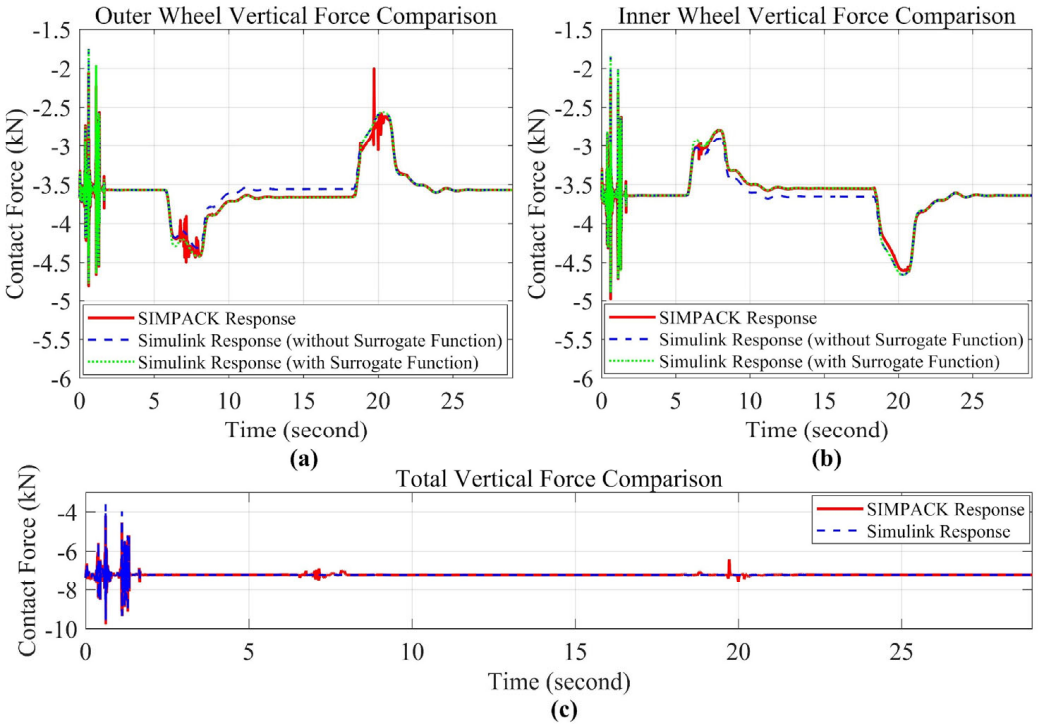


Figure 13. Comparison of vertical wheel forces for 25 km/h and 300 m curve radius: (**a**) outer wheel vertical force comparison; (**b**) inner wheel vertical force comparison; (**c**) total vertical force comparison.

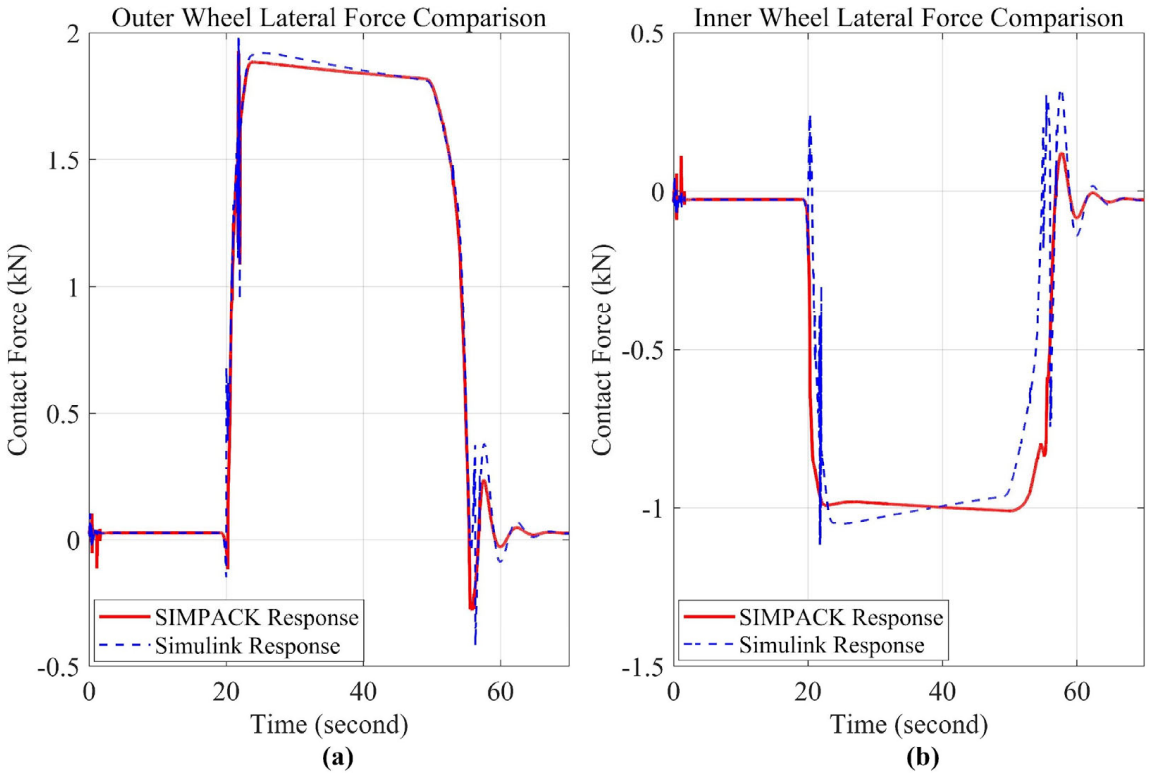


Figure 14. Comparison of lateral wheel forces for 15 km/h and 89 m curve radius: (**a**) outer wheel lateral force comparison; (**b**) inner wheel lateral force comparison.

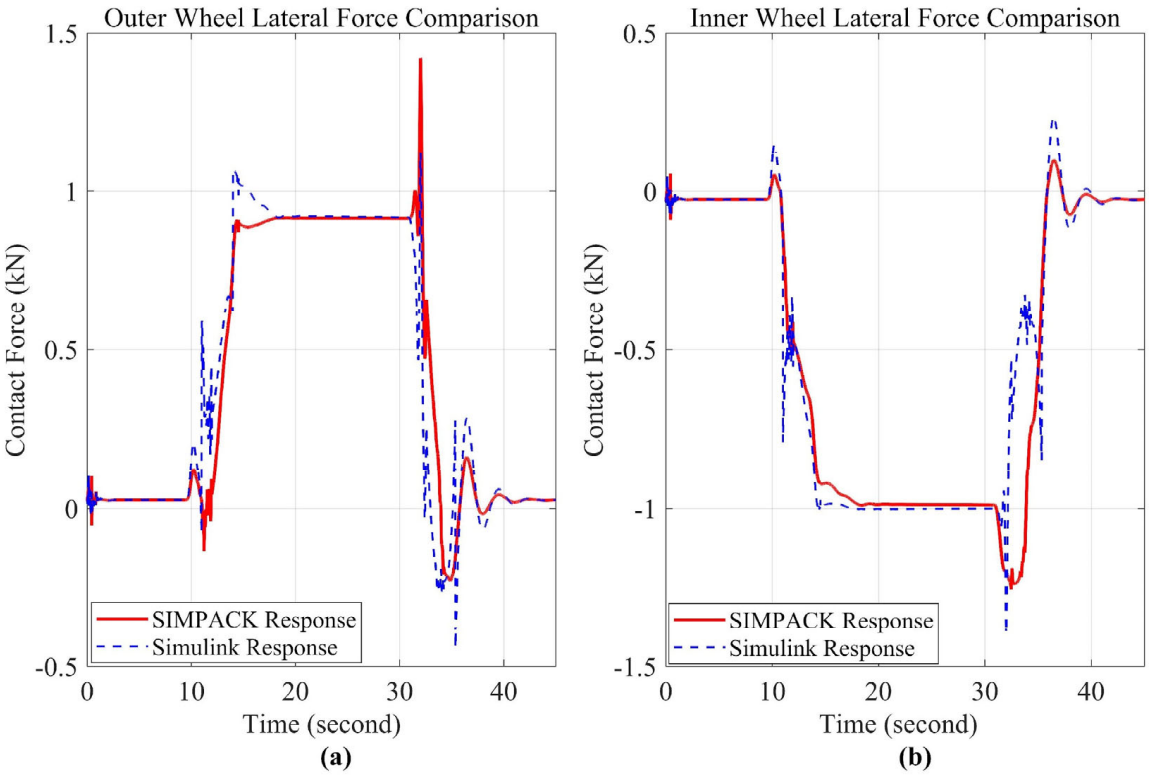


Figure 15. Comparison of lateral wheel forces for 15 km/h and 300 m curve radius: (**a**) outer wheel lateral force comparison; (**b**) inner wheel lateral force comparison.

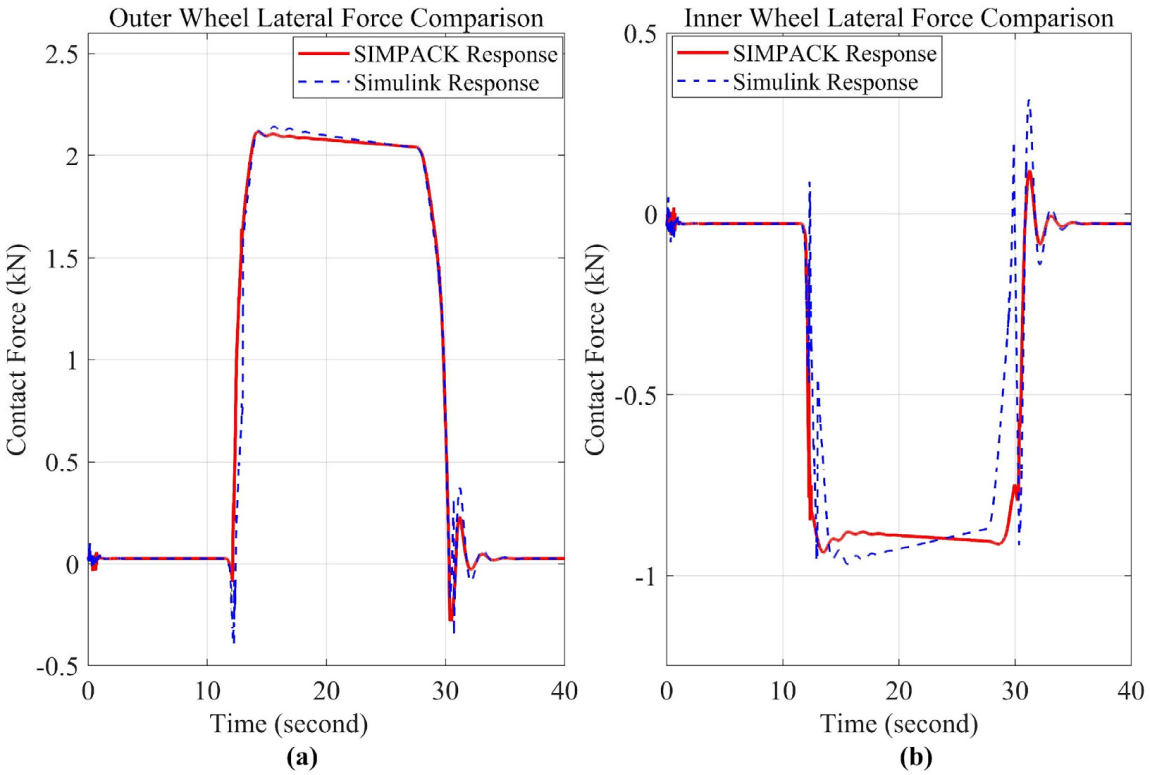


Figure 16. Comparison of lateral wheel forces for 25 km/h and 89 m curve radius: (**a**) outer wheel lateral force comparison; (**b**) inner wheel lateral force comparison.

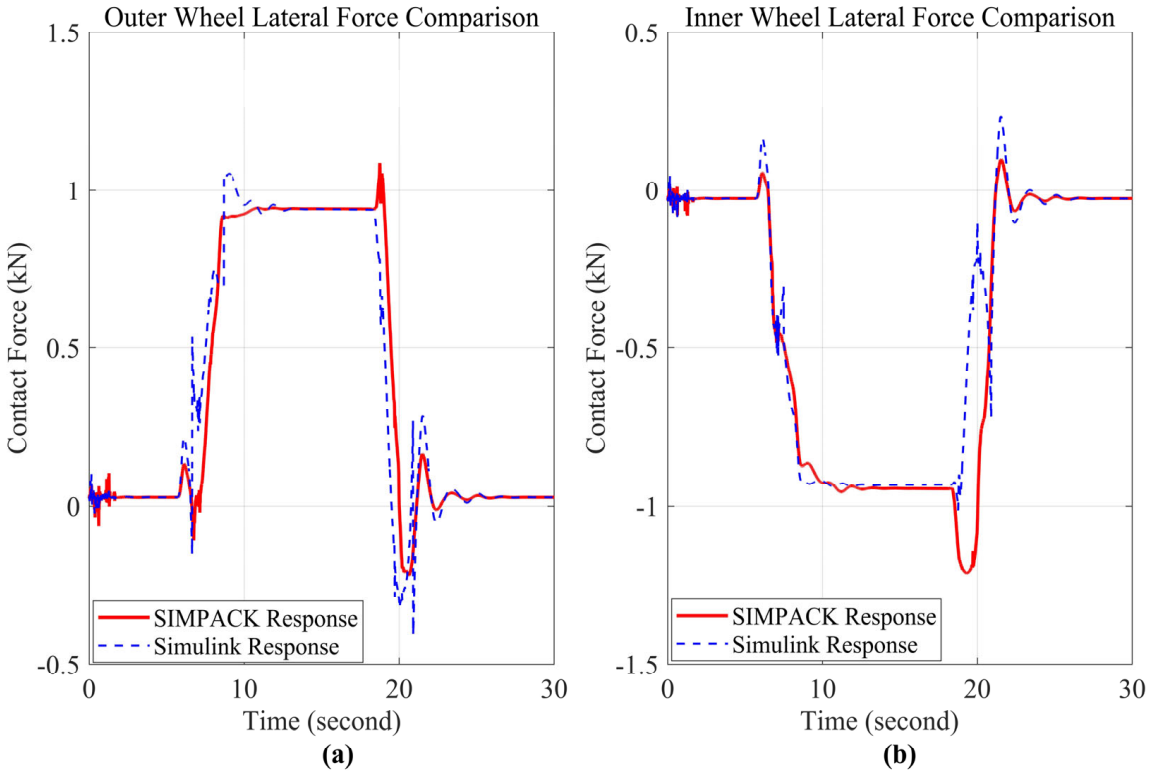


Figure 17. Comparison of lateral wheel forces for 25 km/h and 300 m curve radius: (**a**) outer wheel lateral force comparison; (**b**) inner wheel lateral force comparison.

The estimation of vertical contact forces is inherently less challenging than that of lateral forces; consequently, high accuracy is achieved even without surrogate functions (SFs), resulting in a relatively modest contribution from the SFs. Nevertheless, the proposed method consistently delivers superior performance in curved sections, achieving agreement levels exceeding 98% with excellent consistency across all scenarios.

Table 5. Comparison of outer and inner wheel vertical force simulation results.

Simulation Scenarios		Vertical Contact Force Agreement with SIMPACK Data (%)											
		Tangent Track				Curve				Total Track			
		Without SF		With SF		Without SF		With SF		Without SF		With SF	
		Out	In	Out	In	Out	In	Out	In	Out	In	Out	In
15 km/h	R = 89 m	99.9	99.9	99.9	99.9	95.3	95.0	98.2	98.2	96.3	96.0	98.5	98.6
	R = 300 m	99.9	99.9	99.9	99.9	96.8	95.8	98.6	98.5	97.6	96.8	98.9	98.9
25 km/h	R = 89 m	99.8	99.8	99.8	99.8	94.3	94.7	99.5	99.5	95.6	95.9	99.6	99.6
	R = 300 m	99.8	99.7	99.8	99.7	97.3	97.4	99.2	99.5	98.1	98.1	99.4	99.6

Figures 14–17 compare the outer and inner wheel lateral contact force values obtained from SIMPACK with those calculated using the developed distribution equations. The consistency ratios for the outer and inner wheel lateral contact forces are presented in Table 6.

Table 6. Comparison of distributed lateral force results obtained from MBCM and SIMPACK Simulations.

Simulation Scenarios		Distributed Lateral Force Using MBCM Agreement with SIMPACK Data (%)					
		Tangent Track		Curve		Total Track	
		Out	In	Out	In	Out	In
15 km/h	R = 89 m	99.9	99.9	98.2	90.1	98.8	93.4
	R = 300 m	99.9	99.9	94.9	93.6	96.8	96.0
25 km/h	R = 89 m	99.9	99.8	97.8	91.3	98.6	94.3
	R = 300 m	99.8	99.7	94.4	94.2	95.8	95.7

The proposed method (MBCM) achieves near-perfect accuracy on tangent track ($\geq$99.7%), maintains at least 90.1% agreement even under the most severe sharp-curve conditions (inner rail, R = 89 m), and never falls below 93.4% accuracy over mixed tangent–curve track sections, thereby demonstrating exceptional reliability across the full spectrum of operating scenarios.

4. Discussion

The application flowchart of the approach proposed for the first time in this study, which exhibits high agreement with simulation results obtained under identical conditions using the SIMPACK model, is presented in Figure 18.

As evident from Figure 18, the proposed method is applicable to all railway vehicles. However, certain coefficients ($k_{1(i,d,id,dd)}$, $k_{2(i,d,id,dd)}$, $k_{3(i,d)}$) used in Equations (29)–(32) have been determined specifically for the dynamics of ITA. Additionally, the validation is limited to urban rail transit operations within the city. The simulation scenarios considered only the low speeds (15–25 km/h) permitted for trams during sharp curve transitions. Consequently, the applicability of the proposed method to high-speed trains, which have

substantially different dynamic characteristics, has not yet been verified. This constitutes a critical limitation of the current study and is left as an open avenue for future research.

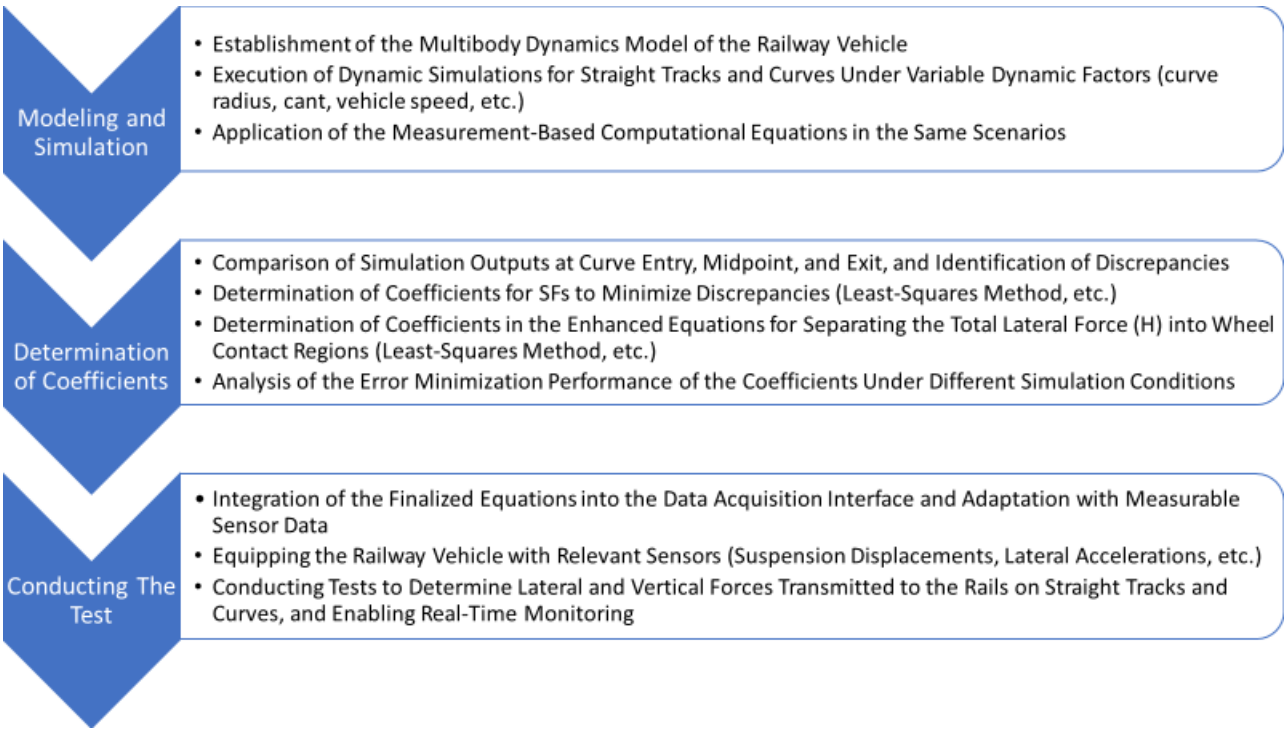


Figure 18. Flowchart of the application of the developed method.

For high-accuracy application of the proposed method to different vehicles, simulations aligned with the flowchart in Figure 18 must be performed, time-varying error quantities on straight tracks and various curves analyzed, and common coefficients that minimize errors derived. In the calibration of surrogate functions and decomposition equations, the broadest possible parameter space should be incorporated by taking into account the actual operating conditions of the vehicle and track dynamics under study. Defining the boundaries of the vehicle speed, curve radius, and cant deficiency ranges within the prediction algorithm matrix in accordance with actual operating conditions will minimize the safety risks associated with the real-world deployment of the proposed method. In this study, the transition speeds (15, 20, and 25 km/h) and corresponding cant conditions were considered for the critical curves on the Topkapı–Mescid-i Selam line of ITA, which consists of three different curve radii (89 m, 240 m, and 300 m). To avoid unnecessarily lengthening the manuscript, simulation results are presented only for the boundary values of these parameters.

Although the method requires pre-test simulation and analysis efforts, it offers a more practical and cost-effective alternative compared to instrumented wheelset applications. Table 7 provides a systematic comparison between the instrumented wheelset method and the MBCM developed in this study.

Although the instrumented wheelset serves as a traditional standard offering high accuracy in laboratory and validation tests for dedicated vehicles, its high cost, complex installation, and limited durability render it unsuitable for fleet-wide applications. In contrast, the MBCM provides a low-cost, practical, and fully compatible alternative for online monitoring using existing vehicle sensors, achieving over 90% accuracy and demonstrating the potential to replace instrumented wheelset applications. Through SFs and distribution equations, this method delivers reliable results for real-time data tracking, proactive

maintenance, and safety inspections, offering accuracy comparable to the instrumented wheelset in compliance with standards (EN 14363, UIC 518).

Table 7. Comparison of the IWS application with the MBCM developed in this study.

Criterion	Instrumented Wheelset (IWS)	Measurement-Based Computational Method
Basic Principle	Direct strain measurement using strain gauges attached to the wheel hub; contact forces are calculated in real time.	Indirect estimation based on analytical equations derived from Newton's laws using data obtained from sensors (accelerometer, suspension displacement, speed) placed on the vehicle.
Accuracy/Consistency	High accuracy (under calibrated laboratory conditions). Directly measures the actual contact force. Accuracy depends on the quality of the strain gauge application.	High consistency (verified with SIMPACK). Effects such as creep and profile change are compensated for with an SF.
Cost	Requires high cost and fixed facilities. Wheel modification, calibration test system, transportation, etc.	Inexpensive sensors such as accelerometers and linear potentiometers are used. No telemetry systems are required. There is a cost for preliminary modeling, simulation, and analysis. The total cost is approximately 1% of that for instrumented wheelset applications.
Installation and Applicability	Wheel removal, strain gauge bonding, wiring, and waterproofing. Requires calibration in a fixed facility using a dedicated test system. The instrumented wheelset bogie is transported to the test site. Preparation, and installation time is lengthy. Telemetry measurement systems are required.	Applicable to every vehicle, no permanent installation required. Small sensors and data acquisition equipment are easy to transport, with short installation time.
Real-Time Monitoring	Direct measurement; strain gauge data is processed, enabling online monitoring.	Direct measurement is used in the equations, enabling instantaneous force values and online monitoring.
Flexibility (Different Vehicle/Line)	Each vehicle type requires specific wheels.	Dynamic system parameters (mass, inertia, suspension stiffness and damping values, etc.) must be known for each vehicle. The coefficients in the equations developed for each vehicle type need to be estimated from error functions obtained through simulations. The method is applicable to all vehicle types following this workflow.
Data Processing and Storage	High sampling rate (1–5 kHz), large data volume, specialized DAQ system.	10–100 Hz is sufficient, low data volume, cloud-compatible.

5. Conclusions

This study has developed a novel MBCM to determine the vertical and lateral wheel–rail contact forces transmitted from railway vehicles to the rails. Addressing a significant gap in the literature, an innovative approach for the analytical distribution of lateral contact forces has been proposed. Initially, analytical equations based on Newton's second law were derived to calculate contact forces in the wheel–rail interface for vehicles operating on straight tracks and curves, yielding expressions for vertical and total lateral contact forces. Unlike existing approaches in the literature, SFs sensitive to variable parameters such as curve radius, vehicle speed, and cant deficiency were introduced for the first time in this study to mitigate deviations arising from simplifying assumptions, including the neglect of wheel diameter variation and creep effects. These functions were integrated into the equations. Furthermore, in curved sections, the total lateral force on the wheelset was distributed into inner and outer wheel contact regions, accounting for vertical load

variations and sensitivity to parameters that may change along the track, such as curve radius, speed, and cant.

To validate the method's accuracy, SIMPACK—a multibody dynamics simulation software widely recognized for its reliability—was employed. Simulations were conducted using the ITA model produced by Metro Istanbul A.Ş. for both straight-track and curved-track scenarios. The analytical equations were implemented in MATLAB/Simulink, and the resulting outputs were compared with SIMPACK reference results. The comparisons demonstrated over 99% consistency in straight-track scenarios, while deviations of 4–6% were observed in curves. These deviations were eliminated through regression-based calibration of the SFs, elevating consistency to over 98% in all scenarios (Tables 4 and 5). In the final stage, analytical equations based on measurable parameters were developed to distribute the total lateral force into outer and inner wheel components. The proposed MBCM delivers near-perfect agreement ($\geq$99.7%) on tangent track, sustains no less than 90% accuracy even in the most demanding sharp-curve cases, and consistently maintains above 93.4% agreement across combined tangent-and-curve track sections, thereby confirming its outstanding robustness and reliability throughout the entire range of operational conditions.

Although the method requires regression analysis dependent on simulation environments like SIMPACK, its reliance solely on measurable parameters offers significant advantages, including low cost, compatibility with existing vehicle sensors, and practical applicability. By enabling real-time data monitoring, the approach facilitates predictive maintenance and proactive decision-support mechanisms.

In addition to presenting a novel methodological contribution to the literature, this study introduces an innovative perspective that has the potential to transform current railway industry practices in maintenance planning and operational safety. Given that the proposed method is intended for a safety-critical application, its experimental validation through field tests remains essential. Future work should compare the method's predictions either with pointwise wheel–rail forces measured using strain gauges mounted on the rails, with results from the wayside method, and/or with higher-speed measurements obtained via the IWS technique. Such rigorous field validation will be indispensable to confirm the method's reliability and to facilitate its practical adoption in the industry.

Author Contributions: Validation, resources, visualization, writing—original draft preparation, software, investigation, data curation, N.B.; methodology, conceptualization, formal analysis, writing—review and editing, supervision, project administration, funding acquisition, M.M. All authors have read and agreed to the published version of the manuscript.

Funding: This research was funded by the THE SCIENTIFIC AND TECHNICAL RESEARCH COUNCIL OF TURKEY (TUBITAK) through the Program for Scientific and Technological Research Projects (1001), grant number 222M001.

Data Availability Statement: The data presented in this study are available on request from the corresponding author. The data are not publicly available due to their large volume and the ongoing nature of related research projects.

Acknowledgments: During the preparation of this manuscript, the authors used GROK 4.1 xAI for the purposes of solely for improving the English grammar of sentences. The authors have reviewed and edited the output and take full responsibility for the content of this publication.

Conflicts of Interest: The authors declare no conflicts of interest. The funders had no role in the design of the study; in the collection, analyses, or interpretation of data; in the writing of the manuscript; or in the decision to publish the results.

Abbreviations

The following abbreviations are used in this manuscript:

ITA	Local Istanbul Tramway
IWS	Instrumented Wheelset
MBCM	Measurement-Based Computational Method
SF	Surrogate Function

Appendix A

Table A1. Nomenclature.

Symbol	Description
A	Independent variables matrices
b	Relative error matrices
β_{ti}	Lateral rolling angular displacement of the bogie (rotation on the y-axis)
$\dot{\beta}_{ti}$	Lateral rolling angular velocities of the bogie (rotation on the y-axis)
d	Cant deficiency
F_{syi}	Total primary lateral suspension force
$F_{sy_{in}}$, $F_{sy_{out}}$	Lateral primary suspension forces for inner and outer wheel
$F_{sz_{in}}$, $F_{sz_{out}}$	Vertical primary suspension forces for inner and outer wheel
$F_{sz_{static}}$	Static external load applied to the vehicle at rest
$F_{y_{in}}$, $F_{y_{out}}$	Lateral contact forces for inner and outer wheel
F_{y_v}	Lateral surrogate function
$F_{z_{in}}$, $F_{z_{out}}$	Vertical contact forces for inner and outer wheel
$F_{z_{out,f}}$, $F_{z_{in,f}}$	The final outer and inner vertical wheel force equation obtained by integrating the outer and inner vertical surrogate functions into the outer and inner vertical wheel force equations
$F_{z_{v(out,in)}}$	Vertical surrogate functions for outer and inner wheel
$\varnothing_{se}$	The superelevation angle resulting from the height difference between the outer and inner rails
$\varnothing_{wi}$, $\varnothing_{ti}$	Longitudinal rolling angular displacements of the wheelset and bogie (rotation on the x-axis)
$\dot{\varnothing}_{wi}$, $\dot{\varnothing}_{ti}$	Longitudinal rolling angular velocities of the wheelset and bogie (rotation on the x-axis)
G	Gravitational acceleration
H	Total lateral wheel–rail contact force
H_f	The final total lateral wheel force equation obtained by integrating the lateral surrogate function into the total lateral wheel force equation
h_t	Vertical distance between bogie center and wheelset center distance between bogie center and wheelset center
K_{py}, C_{py}	Lateral spring and damping coefficient for primary suspension
K_{pz}, C_{pz}	Vertical spring and damping coefficient for primary suspension
k_t, g_t, z_t	Lateral surrogate function weighting coefficients
k_{td}, g_{td}, z_{td}	Vertical surrogate function weighting coefficients
k_{1d}, k_{2d}, k_{1i}, k_{2i}	Weighting coefficients in the outer and inner wheel lateral force equation on a tangent track
k_{1dd}, k_{2dd}, k_{3d},k_{1id}, k_{2id}, k_{3i}	Weighting coefficients in the outer and inner wheel lateral force equation on a curved line
L_c	Lateral distance between the two wheel–rail contact points of a wheelset
L_s	Lateral distance between the primary suspensions connecting the bogie and the wheelset
L_1	Half the longitudinal distance between the front and rear wheelsets of the bogie
m_w	Wheelset mass
ψ_{ti}	Yaw rolling angular displacement of the bogie (rotation on the z-axis)
$\dot{\psi}_{ti}$	Yaw rolling angular velocities of the bogie (rotation on the z-axis)
R	Curve radius
r_0	Nominal rolling radius of the wheel
V	Vehicle velocity
y_{wi}, y_{ti}	Linear lateral displacements of the wheelset and bogie
$\dot{y}_{wi}$, $\dot{y}_{ti}$	Linear lateral velocities of the wheelset and bogie
z_{wi}, z_{ti}	Linear vertical displacements of the wheelset and bogie
$\dot{z}_{wi}$, $\dot{z}_{ti}$	Linear vertical velocities of the wheelset and bogie
$\ddot{z}_{wi}$, $\ddot{y}_{wi}$	Vertical and lateral linear accelerations of the wheelset

References

1. *EN 14363:2016+A2:2022*; Railway Applications—Testing and Simulation for the Acceptance of Running Characteristics of Railway Vehicles—Running Behaviour and Stationary Tests. European Committee for Standardization (CEN): Brussels, Belgium, 2022.
2. *UIC Code 518:2009*; Testing and Approval of Railway Vehicles from the Point of View of Their Dynamic Behaviour—Safety—Track Fatigue—Ride Quality. International Union of Railways (UIC): Paris, France, 2009.
3. Wu, P.; Zhang, F.; Wang, J.; Wei, L.; Huo, W. Review of wheel-rail forces measuring technology for railway vehicles. *Adv. Mech. Eng.* **2023**, *15*, 16878132231158991. [CrossRef]
4. Kanehara, H.; Fujioka, T. Measuring rail/wheel contact points of running railway vehicles. *Wear* **2002**, *253*, 275–283. [CrossRef]
5. Magel, E.; Tajaddini, A.; Trosino, M.; Kalousek, J. Traction, forces, wheel climb and damage in high-speed railway operations. *Wear* **2008**, *265*, 1446–1451. [CrossRef]
6. Ronasi, H.; Nielsen, J.C. Inverse identification of wheel–rail contact forces based on observation of wheel disc strains: An evaluation of three numerical algorithms. *Veh. Syst. Dyn.* **2013**, *51*, 74–90. [CrossRef]
7. Gupta, R.; Bharti, P. Evaluation of wheel load & lateral forces, using lateral & vertical force measurement wheel in dynamic condition at rail wheel contact point. *Int. J. Eng. Res. Technol.* **2015**, *4*, 894–902. [CrossRef]
8. Urda, P.; Muñoz, S.; Aceituno, J.F.; Escalona, J.L. Wheel-rail contact force measurement using strain gauges and distance lasers on a scaled railway vehicle. *Mech. Syst. Signal Process.* **2020**, *138*, 106555. [CrossRef]
9. Papini, S.; Pugi, L.; Rindi, A.; Meli, E. An integrated approach for the optimization of wheel–rail contact force measurement systems. *J. Mod. Transp.* **2013**, *21*, 95–102. [CrossRef]
10. Ronasi, H.; Johansson, H.; Larsson, F. Identification of wheel–rail contact forces based on strain measurements, an inverse scheme and a finite-element model of the wheel. *Proc. Inst. Mech. Eng. Part F J. Rail Rapid Transit* **2014**, *228*, 343–354. [CrossRef]
11. Bagheri, V.R.; Tehrani, P.H.; Younesian, D. Optimal strain gauge placement in instrumented wheelset for measuring wheel-rail contact forces. *Int. J. Precis. Eng. Manuf.* **2017**, *18*, 1519–1527. [CrossRef]
12. Bižić, M.; Petrović, D. Design of instrumented wheelset for measuring wheel-rail interaction forces. *Metrol. Meas. Syst.* **2023**, *30*, 563–579. [CrossRef]
13. Cai, Y.; Chen, B.; Chang, C. Research on the strain gauge mounting scheme of track wheel force measurement system based on high-speed wheel/rail relationship test rig. *Railw. Sci.* **2024**, *3*, 503–513. [CrossRef]
14. Gomez, E.; Giménez, J.; Alonso, A. Method for the reduction of measurement errors associated to the wheel rotation in railway dynamometric wheelsets. *Mech. Syst. Signal Process.* **2011**, *25*, 3062–3077. [CrossRef]
15. Bižić, M.B.; Petrović, D.Z.; Tomić, M.C.; Djinović, Z.V. Development of method for experimental determination of wheel–rail contact forces and contact point position by using instrumented wheelset. *Meas. Sci. Technol.* **2017**, *28*, 075902. [CrossRef]
16. Ren, Y.; Chen, J. A new method for wheel–rail contact force continuous measurement using instrumented wheelset. *Veh. Syst. Dyn.* **2019**, *57*, 269–285. [CrossRef]
17. Nielsen, J.C. High-frequency vertical wheel–rail contact forces—Validation of a prediction model by field testing. *Wear* **2008**, *265*, 1465–1471. [CrossRef]
18. Gullers, P.; Andersson, L.; Lundén, R. High-frequency vertical wheel–rail contact forces—Field measurements and influence of track irregularities. *Wear* **2008**, *265*, 1472–1478. [CrossRef]
19. Ham, Y.-S.; Lee, D.-H.; Kwon, S.-J.; You, W.-H.; Oh, T.-Y. Continuous measurement of interaction forces between wheel and rail. *Int. J. Precis. Eng. Manuf.* **2009**, *10*, 35–39. [CrossRef]
20. Bagheri, V.R.; Younesian, D.; Tehrani, P.H. A new methodology for the estimation of wheel–rail contact forces at a high-frequency range. *Proc. Inst. Mech. Eng. Part F J. Rail Rapid Transit* **2018**, *232*, 2353–2370. [CrossRef]
21. Hondo, T.; Kuniyuki, S.; Tanaka, T.; Suzuki, M. Method for measuring lateral force utilizing shear strains inside wheel load measuring holes of instrumented wheelset. *Q. Rep. RTRI* **2022**, *63*, 139–144. [CrossRef]
22. Jin, X. A measurement and evaluation method for wheel-rail contact forces and axle stresses of high-speed train. *Measurement* **2020**, *149*, 106983. [CrossRef]
23. Matsumoto, A.; Sato, Y.; Ohno, H.; Tomeoka, M.; Matsumoto, K.; Kurihara, J.; Ogino, T.; Tanimoto, M.; Kishimoto, Y.; Sato, Y. A new measuring method of wheel–rail contact forces and related considerations. *Wear* **2008**, *265*, 1518–1525. [CrossRef]
24. Matsumoto, A.; Sato, Y.; Ohno, H.; Shimizu, M.; Kurihara, J.; Tomeoka, M.; Saitou, T.; Michitsuji, Y.; Tanimoto, M.; Sato, Y. Continuous observation of wheel/rail contact forces in curved track and theoretical considerations. *Veh. Syst. Dyn.* **2012**, *50*, 349–364. [CrossRef]
25. Matsumoto, A.; Sato, Y.; Ohno, H.; Shimizu, M.; Kurihara, J.; Saitou, T.; Michitsuji, Y.; Matsui, R.; Tanimoto, M.; Mizuno, M.-A. Actual states of wheel/rail contact forces and friction on sharp curves–continuous monitoring from in-service trains and numerical simulations. *Wear* **2014**, *314*, 189–197. [CrossRef]
26. Wei, L.; Zeng, J.; Wu, P.; Gao, H. Indirect method for wheel–rail force measurement and derailment evaluation. *Veh. Syst. Dyn.* **2014**, *52*, 1622–1641. [CrossRef]

27. Strano, S.; Terzo, M. On the real-time estimation of the wheel-rail contact force by means of a new nonlinear estimator design model. *Mech. Syst. Signal Process.* **2018**, *105*, 391–403. [CrossRef]
28. Mal, K.; Hussain, I.; Chowdhry, B.S.; Memon, T.D. Extended Kalman filter for estimation of contact forces at wheel-rail interface. *3C Tecnol.* **2020**, *2020*, 279–301. [CrossRef]
29. Zhao, A.; Huang, J.; Sun, J.-Q. Estimation of wheel–rail structural interactions from motion signals of high-speed train bogie. *Int. J. Dyn. Control* **2023**, *11*, 1609–1620. [CrossRef]
30. Sun, Y.Q.; Cole, C.; Spiryagin, M. Monitoring vertical wheel–rail contact forces based on freight wagon inverse modelling. *Adv. Mech. Eng.* **2015**, *7*, 1687814015585431. [CrossRef]
31. Zhu, T.; Wang, X.-R.; Fan, Y.-W.; Wang, M.-M.; Zhang, J.-K.; Xiao, S.-N.; Yang, G.-W.; Yang, B. A time domain method for wheel-rail force identification of rail vehicles. *Veh. Syst. Dyn.* **2022**, *60*, 790–809. [CrossRef]
32. Bosso, N.; Zampieri, N. A Novel Analytical Method to Calculate Wheel-Rail Tangential Forces and Validation on a Scaled Roller-Rig. *Adv. Tribol.* **2018**, *2018*, 7298236. [CrossRef]
33. Pires, A.; Mendes, G.; Santos, G.; Dias, A.; Santos, A. Indirect identification of wheel rail contact forces of an instrumented heavy haul railway vehicle using machine learning. *Mech. Syst. Signal Process.* **2021**, *160*, 107806. [CrossRef]
34. Gadhave, R.; Vyas, N. Rail-wheel contact forces and track irregularity estimation from on-board accelerometer data. *Veh. Syst. Dyn.* **2022**, *60*, 2145–2166. [CrossRef]
35. Majumder, S.; Singh, A.; Singh, A.; Karpenko, M.; Sharma, H.K.; Mukhopadhyay, S. On the analytical study of the service quality of Indian Railways under soft-computing paradigm. *Transport* **2024**, *39*, 54–63. [CrossRef]
36. Zhu, T.; Wang, X.; Wu, J.; Zhang, J.; Xiao, S.; Lu, L.; Yang, B.; Yang, G. Comprehensive identification of wheel-rail forces for rail vehicles based on the time domain and machine learning methods. *Mech. Syst. Signal Process.* **2025**, *222*, 111635. [CrossRef]
37. Liu, H.; Song, L.; Xu, L.; Yu, Z. Identification of wheel-rail forces on high-speed railways based on physical model and hybrid recursive neural networks. *Eng. Struct.* **2025**, *338*, 120547. [CrossRef]
38. Cortis, D.; Bruner, M.; Malavasi, G.; Rossi, S.; Catena, M.; Testa, M. Estimation of the wheel-rail lateral contact force through the analysis of the rail web bending strains. *Measurement* **2017**, *99*, 23–35. [CrossRef]
39. Bulduk, N.; Metin, M.; Marabaoğlu, D. Development of a Measurement-Based Computational Method for Determination of Vehicle-Induced Road Loads on Railways and Its Analysis in a Simulation Environment. *Demiryolu Mühendisliği* **2025**, *21*, 39–60. [CrossRef]

Disclaimer/Publisher's Note: The statements, opinions and data contained in all publications are solely those of the individual author(s) and contributor(s) and not of MDPI and/or the editor(s). MDPI and/or the editor(s) disclaim responsibility for any injury to people or property resulting from any ideas, methods, instructions or products referred to in the content.